

## A polarization study of the supernova remnant CTB 80

Xiang-Hua Li (李向华)<sup>1</sup>, Xiao-Hui Sun (孙晓辉)<sup>1</sup>, Wolfgang Reich<sup>2</sup> and Xu-Yang Gao (高旭阳)<sup>3,4</sup>

<sup>1</sup> Department of Astronomy, Yunnan University, and Key Laboratory of Astroparticle Physics of Yunnan Province, Kunming 650091, China; [xhsun@ynu.edu.cn](mailto:xhsun@ynu.edu.cn)

<sup>2</sup> Max-Planck-Institut für Radioastronomie, Auf dem Hügel 69, 53121 Bonn, Germany

<sup>3</sup> National Astronomical Observatories, Chinese Academy of Sciences, Beijing 100101, China

<sup>4</sup> CAS Key Laboratory of FAST, National Astronomical Observatories, Chinese Academy of Sciences, Beijing 100101, China

Received 2020 April 23; accepted 2020 July 16

**Abstract** We present a radio polarization study of the supernova remnant CTB 80 based on images at 1420 MHz from the Canadian Galactic Plane Survey, at 2695 MHz from the Effelsberg survey of the Galactic plane and at 4800 MHz from the Sino-German  $\lambda 6$  cm polarization survey of the Galactic plane. We obtained a rotation measure (RM) map using polarization angles at 2695 MHz and 4800 MHz as the polarization percentages are similar at these two frequencies. RM exhibits a transition from positive values to negative values along one of the shells hosting the pulsar PSR B1951+32 and its pulsar wind nebula. The reason for the change in sign remains unclear. We identified a partial shell structure, which is bright in polarized intensity but weak in total intensity. This structure could be part of CTB 80 or part of a new supernova remnant unrelated to CTB 80.

**Key words:** ISM: supernova remnants — ISM: magnetic fields — polarization — techniques: polarimetric

### 1 INTRODUCTION

CTB 80 is a prominent radio source with a complex morphology consisting of a bright central source embedded in a plateau and extended ridges or shells. Velusamy & Kundu (1974) suggested that CTB 80 is a supernova remnant (SNR) based on its non-thermal spectrum and high polarization percentage of 15%–20% at  $\lambda 11$  cm. Angerhofer et al. (1981) confirmed that CTB 80 is an SNR from high-resolution observations and proposed that the central source probably is a Crab-like SNR, because it is highly polarized and its spectrum is flat. Follow-up X-ray (Becker et al. 1982) and radio (Strom et al. 1984) observations of the central source implied the presence of a pulsar, which was later discovered by Kulkarni et al. (1988) as PSR B1951+32. The pulsar has a dispersion measure (DM) of about  $45 \text{ cm}^{-3} \text{ pc}$  (Hobbs et al. 2004) and a rotation measure (RM) of  $-182 \pm 8 \text{ rad m}^{-2}$  (Weisberg et al. 2004).

The origin of the morphology of CTB 80 has been puzzling since its identification decades ago. Infrared, H I and X-ray observations led to the scenario of PSR

B1951+32 and its associated pulsar wind nebula (PWN) rejuvenating an old SNR shell (Fesen et al. 1988; Koo et al. 1993; Safi-Harb et al. 1995). Castelletti & Dubner (2005) derived a map of spectral indices utilizing observations at 610 MHz and 1380 MHz conducted by Castelletti et al. (2003), and found that spectra are flat towards the central PWN area and gradually steepen further away from the PWN area along the shells. This supports that the high-energy electrons accounting for emission from the shells are supplied by the pulsar and its PWN.

One of the keys to understanding CTB 80 is the magnetic field, which can be studied by radio polarimetry. Mantovani et al. (1985) conducted polarization observations of CTB 80 at 1410 MHz, 1720 MHz, 2695 MHz and 4750 MHz, and obtained the orientation of magnetic fields projected onto the plane of the sky after RM correction. They found that the magnetic field is well ordered, parallel to the eastern and southwestern shell but virtually perpendicular to the northern shell, which motivated them to put forward an alternative scenario of two SNR shells interacting.

The distance to CTB 80 varies with different measurement methodologies. Based on the DM of PSR B1951+32, the distance is either 1.4 kpc (Kulkarni et al. 1988) or  $3 \pm 2$  kpc (Yao et al. 2017) depending on the thermal electron density model. The optical observations yield a color excess  $E(B - V)$  of about 0.8, suggesting a distance of about 2.5 kpc (Blair et al. 1984). Shan et al. (2018) derived an extinction  $A_V$  from the color excess and obtained a distance of 4.6 kpc. From X-ray observations, Mavromatakis et al. (2001) determined a column density of H I and then derived a color excess of about 0.4, which they attributed to foreground absorption. This means that the extra color excess of about 0.4 is from absorption local to the SNR. Assuming a color excess of about 0.4 from the foreground absorption, the distance is about 2 kpc from the recent three-dimensional (3D) reddening map by Green et al. (2018). The H I observations show an absorption feature at the velocity of about  $12 \text{ km s}^{-1}$  (Koo et al. 1993; Leahy & Ranasinghe 2012). This velocity is less than the terminal velocity and therefore corresponds to two distances: 1.1 – 2.1 kpc and 4.0 – 5.0 kpc after taking into account the velocity dispersion (Leahy & Ranasinghe 2012). To be compatible with most of the measurements, we set a value of 2 kpc for the distance to CTB 80 in this paper, which is also applied to PSR B1951+32.

In this paper, we re-examine CTB 80 with more recent polarization observations of higher quality from the Canadian Galactic Plane Survey (CGPS) at 1420 MHz (Kothés et al. 2006; Landecker et al. 2010), the Effelsberg 2.695-GHz survey of the Galactic plane (Duncan et al. 1999) and the Sino-German  $\lambda 6$  cm polarization survey of the Galactic plane (Xiao et al. 2011). The layout of the paper is as follows. We present the data in Section 2, analysis and discussion on polarization properties in Section 3 and conclusions in Section 4.

## 2 DATA

We focus our analysis on the polarized intensity ( $PI$ ) images of CTB 80 at 1420 MHz, 2695 MHz and 4800 MHz. We also investigate the total intensity ( $I$ ) images at these frequencies as well as that at 408 MHz for the spectrum. All the data are cutouts from published Galactic plane surveys with characteristics listed in Table 1.

At 408 MHz and 1420 MHz, CTB 80 was covered by the CGPS with the synthesis telescope at the Dominion Radio Astrophysical Observatory (Taylor et al. 2003; Landecker et al. 2010; Tung et al. 2017). Images of most of the known SNRs from the survey were presented by Kothés et al. (2006). The resolution is about  $1'$ . The data can be accessed from the Canadian Astronomy

Data Center<sup>1</sup>. The interferometric CGPS data miss large-scale structures and were combined with single-dish data from the Effelsberg 100-m and the Stockert 25-m telescopes at 1420 MHz (Reich 1982; Reich et al. 2004). The maps at 2695 MHz were from the Galactic plane survey conducted by using the Effelsberg 100-m telescope in total intensity (Reich et al. 1990) and in polarization (Duncan et al. 1999), which can be retrieved from the “Survey Sampler” hosted by the Max-Planck-Institut für Radioastronomie<sup>2</sup>. The original resolution is  $4'.3$ . The data at 4800 MHz were from the Sino-German  $\lambda 6$  cm polarization survey of the Galactic plane (Xiao et al. 2011). Maps of large SNRs including CTB 80 from this survey were presented by Gao et al. (2011). The resolution is about  $9'.5$ . The data are also publicly available<sup>3</sup>.

The original images of both  $I$  and  $PI$  for CTB 80 are displayed in Figure 1. The polarized intensity is calculated from Stokes  $Q$  and  $U$  as  $PI = \sqrt{Q^2 + U^2 - \sigma^2}$  (Wardle & Kronberg 1974), where  $\sigma$  is the root mean square (rms) noise in  $Q$  and  $U$ . To highlight the weak diffuse emission, contours are overlaid on the total intensity images. From the total-intensity maps, we can clearly see two bright shell structures, where the pulsar and its PWN are located at the intersection of the two shells. The emission from the PWN is blended with that of the shells. The bright complex at the lower left of the maps contains many individual H II regions which are unrelated to CTB 80 (Anderson et al. 2018). From the polarization images, two shell structures corresponding to those in the total-intensity images are clearly visible at all three frequencies, and are marked as B and C, respectively. Another shell-like structure extends from shell B, as can be seen at 1420 MHz and 4800 MHz. This partial shell structure is marked as A, which manifests as a diffuse patch at 2695 MHz. The total intensity corresponding to shell A is weak at all three frequencies.

## 3 RESULTS AND DISCUSSIONS

We smoothed the maps of  $I$ ,  $Q$  and  $U$  at all the frequencies to a common resolution of  $10'$  for the analyses in this section.

### 3.1 Total Intensity Spectrum

We checked the total-intensity spectra by applying the TT-plot method (Turtle et al. 1962), namely plotting and linearly fitting brightness temperature at one frequency

<sup>1</sup> <https://www.cadc-ccda.hia-ihp.nrc-cnrc.gc.ca/en/cgps/>

<sup>2</sup> <https://www.mpifr-bonn.mpg.de/survey.html>

<sup>3</sup> <http://zmtt.bao.ac.cn/6cm/index.html>

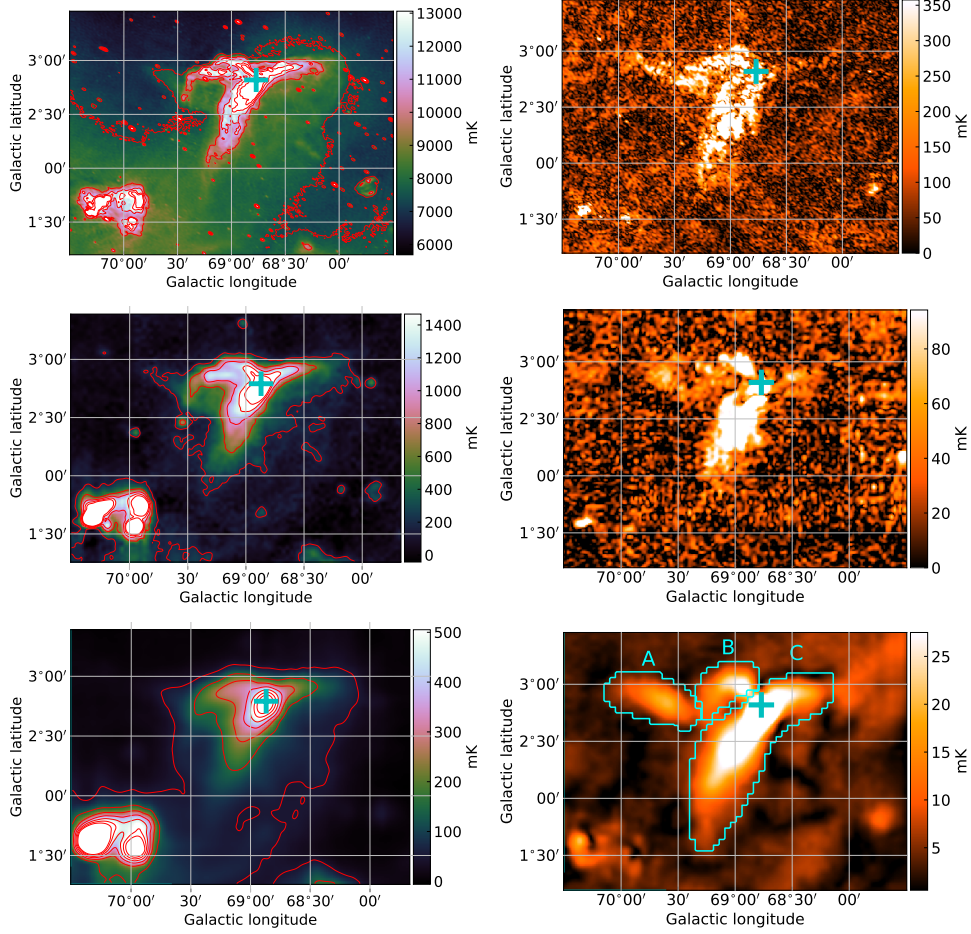


**Fig. 1** Total-intensity images (*left column*) and polarized intensity images (*right column*) of CTB 80 at 1420 MHz (*top*), 2695 MHz (*middle*) and 4800 MHz (*bottom*) at angular resolutions as listed in Table 1. The contour levels start from 7500 mK and increase by 2000 mK at 1420 MHz; start from 200 mK and increase by 400 mK at 2695 MHz; and start from 50 mK and increase by 100 mK at 4800 MHz respectively. All the intensity values are in main beam brightness temperature. The pulsar PSR B1951+32 is marked by a cross in each panel.

**Table 1** Characteristics of the Surveys

Frequency	408 (MHz)	1420 (MHz)	2695 (MHz)	4800 (MHz)
Survey	CGPS	CGPS	Effelsberg survey	Sino-German survey
Telescope	DRAO	DRAO	Effelsberg	Urumqi
Angular resolution	$3'.4 \times 3'.4 \text{ cosec } \delta$	$58'' \times 58'' \text{ cosec } \delta$	$4'.3$	$9'.5$
rms noise, $I$ (mK $T_B$ )	1000	50	20	1
rms noise, $PI$ (mK $T_B$ )		30	13	0.6

The quoted rms-noise values were measured from the area surrounding CTB 80 and are in main beam brightness temperature mK  $T_B$ .

against that at the other frequency to obtain the spectral index  $\beta$  as  $T \propto \nu^\beta$ . The spectral index  $\alpha$  for flux density  $S$ , defined as  $S \propto \nu^\alpha$ , can be obtained as  $\alpha = \beta + 2$ . TT-plots are immune to the influence of constant large-scale background emission, which is critical for weak structures such as shell A. From Figure 1, it can be clearly seen that CTB 80 sits on a plateau of diffuse emission whose influence on the total-intensity spectra can also be eliminated by utilizing TT-plots.

The TT-plot results between 408 MHz and 4800 MHz, and between 1420 MHz and 4800 MHz are featured in Figure 2 for all the three areas. Both shell B and shell C have a brightness temperature spectral index of  $\beta \sim -2.4$  corresponding to a flux density spectral index of  $\alpha \sim -0.4$ , consistent with previous results (Kothes et al. 2006; Gao et al. 2011). For shell structure A, the spectrum is flatter with a brightness temperature spectral index of  $\beta \sim$

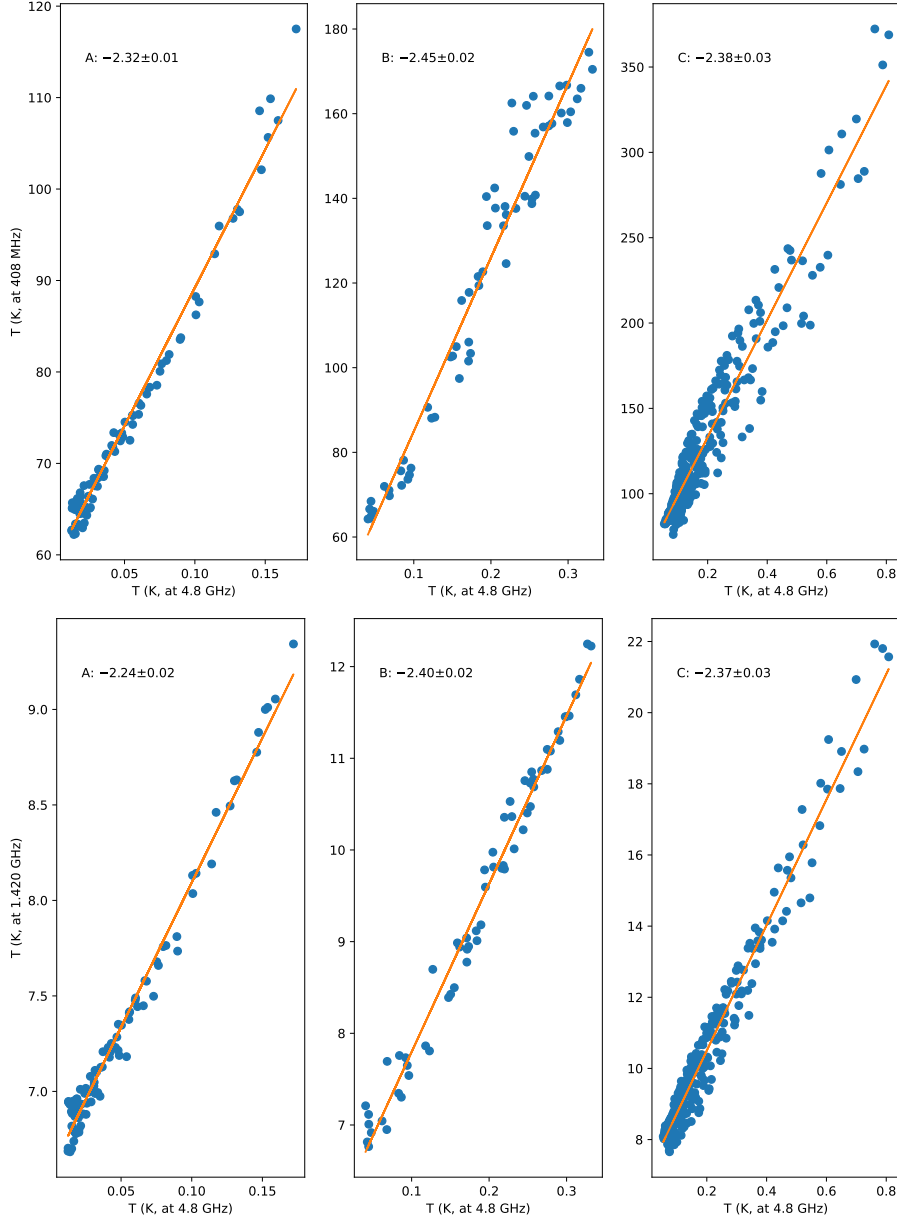


**Fig. 2** TT-plots for total intensities between 408 MHz and 4800 MHz, and between 1420 MHz and 4800 MHz for structures A, B and C, from left to right respectively.

$-2.3$  between 408 MHz and 4800 MHz, and  $\beta \sim -2.2$  between 1420 MHz and 4800 MHz.

### 3.2 Depolarization

The emission encoded in the maps in Figure 1 consists of contributions from CTB 80 and the Milky Way background. The latter is irrelevant and shall be removed for further analysis. For  $Q$  and  $U$  maps, we removed the background emission by subtracting a plane fitted with the values surrounding CTB 80. From these reprocessed  $Q$  and  $U$  maps, we obtained polarized intensity  $PI$  (Fig. 3) and polarization angle as  $\psi = \frac{1}{2} \arctan \frac{U}{Q}$ .

For the total-intensity maps, it is very difficult to exclude the background emission. As a consequence, the polarization percentage defined as  $PC = PI/I$  would have large uncertainties. In order to circumvent this problem, we compare the polarization at different frequencies by considering the relative polarization percentage or the depolarization factor defined as  $DP_\nu = \frac{PI_\nu}{PI_{\nu_0}} \left(\frac{\nu_0}{\nu}\right)^\beta$ , where  $\nu = 1420$  MHz or  $2695$  MHz, and  $\nu_0 = 4800$  MHz. Here we assume that depolarization is the least at 4800 MHz and use  $PI_{4800}$  as the reference. If there is no depolarization, both  $DP_{1420}$  and  $DP_{2695}$  would be around 1.

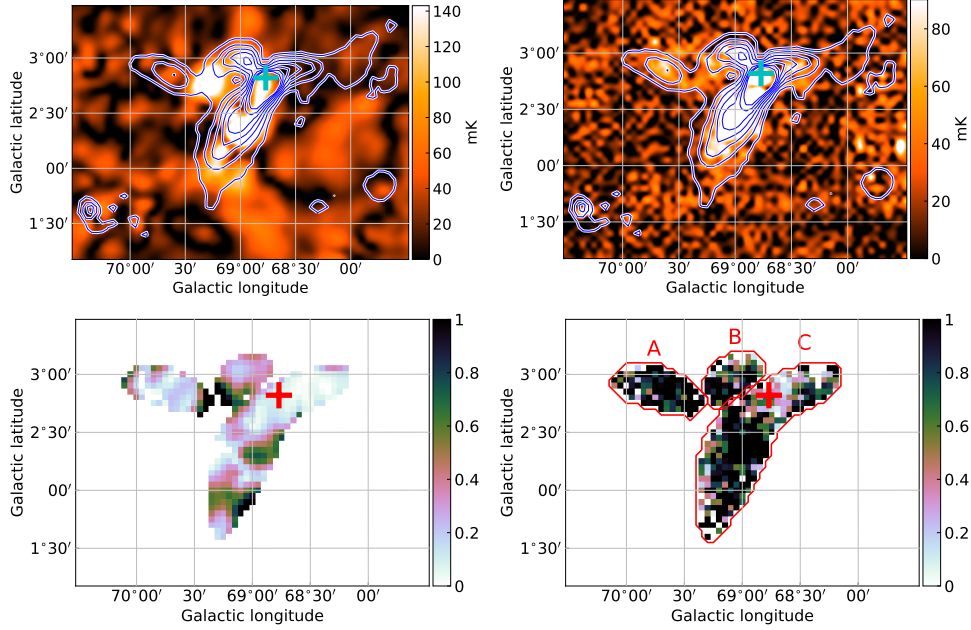


**Fig. 3** Maps of the polarized intensity of CTB 80 at 1420 MHz (*top left panel*) and at 2695 MHz (*top right panel*) at  $10'$  angular resolution, and the distribution of the depolarization factor (see text) at 1420 MHz (*bottom left panel*) and at 2695 MHz (*bottom right panel*). The contours indicating polarized intensity at 4800 MHz run from 6 mK to 42 mK in steps of 6 mK. The pulsar PSR B1951+32 is marked by a cross in all panels.

We calculated  $DP_{1420}$  and  $DP_{2695}$  by using the brightness temperature spectral index from the TT-plots between 1420 MHz and 4800 MHz (Fig. 2), namely  $\beta = -2.24$  for area A,  $\beta = -2.40$  for area B and  $\beta = -2.37$  for area C. The results are depicted in the lower panels of Figure 3.

There is strong depolarization at 1420 MHz. The general morphology of the polarized intensity at 1420 MHz before smoothing resembles that at 4800 MHz (Fig. 1). However, the polarized intensity is largely reduced and the morphology dramatically changes after smoothing because of fluctuation in the polarization angles. There are clear offsets between positions of strong polarized emission at 1420 MHz and that at 4800 MHz, as can be seen from Figure 3. This implies that the polarized emission at 1420 MHz and at 4800 MHz probably originates from different regions. We therefore did not include the polarization data at 1420 MHz for RM calculations.

The polarized intensity at 2695 MHz corresponds well to that at 4800 MHz. Thus, the depolarization factor is around 1 for all areas except for the region near PSR B1951+32 where  $DP_{2695}$  varies from about 0.1 to about 0.7, indicating depolarization towards this region. A detailed discussion on the depolarization mechanisms was provided by Sokoloff et al. (1998). If the depolarization is caused by thermal gas that co-exists with the synchrotron-emitting medium, which is referred to as depth depolariza-

tion, the depolarization factor can be expressed as  $DP_\nu = \frac{\sin(RM\lambda^2)}{\sin(RM\lambda_0^2)} \frac{\lambda_0^2}{\lambda^2}$ . Here the wavelengths  $\lambda$  and  $\lambda_0$  correspond to the frequencies 2695 MHz and 4800 MHz, respectively; and RM is the rotation measure contributed by the whole medium. Given the  $DP_{2695}$  values above for the area near PSR B1951+32, the absolute values of RM fall in the range of  $\sim 120 - \sim 240 \text{ rad m}^{-2}$ . If the depolarization is caused by RM fluctuations  $\sigma_{\text{RM}}$  within the beam, which is referred to as beam depolarization, the depolarization factor can be written as  $DP_\nu = \exp[-2\sigma_{\text{RM}}^2(\lambda^4 - \lambda_0^4)]$ . The values of  $DP_{2695}$  yield the RM fluctuations from  $\sim 35 \text{ rad m}^{-2}$  to  $\sim 85 \text{ rad m}^{-2}$ . However, the RM fluctuations at these levels will cause virtually complete depolarization at 1420 MHz even before smoothing, which contradicts the observations. Therefore, we attribute the observed depolarization around the pulsar area to depth depolarization.

### 3.3 RM Map

The polarization angle varies with wavelength  $\lambda$  because of Faraday rotation, and can be expressed as  $\psi = \psi_0 + \text{RM} \lambda^2$ . RM is equal to the Faraday depth and thus is calculated as  $\text{RM} = 0.81 \int_{\text{source}}^{\text{observer}} n_e B_{\parallel} dl$ , where  $n_e$  is the thermal electron density in  $\text{cm}^{-3}$ ,  $B_{\parallel}$  is the line-of-sight component of the magnetic field in  $\mu\text{G}$ ,  $dl$  is the path length segment along the line of sight in pc and the resultant RM is in  $\text{rad m}^{-2}$ . Positive RMs mean that the

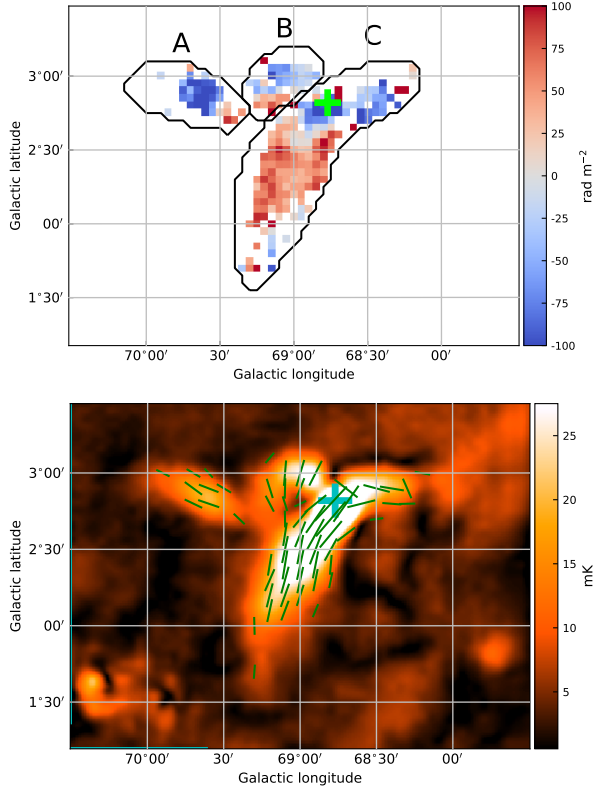


**Fig. 4** RM (top panel) and orientation of transverse magnetic fields indicated by bars overlaid on the polarized-intensity image at 4800 MHz (bottom panel). The length of the bars is proportional to the square root of polarized intensity. The crosses mark the position of PSR B1951+32.

magnetic field points towards the observer. The intrinsic polarization angle  $\psi_0$  is perpendicular to the orientation of the transverse magnetic fields in the source.

We used data at 4800 MHz and 2695 MHz to estimate the rotation measure as  $RM = \frac{\psi_2 - \psi_1}{\lambda_2^2 - \lambda_1^2}$ , where the subscripts 1 and 2 stand for quantities at these two wavelengths, respectively. Because of the  $n\pi$  ambiguity of polarization angles, the resultant RM can differ by an integer multiple of  $\mathcal{R} = \pi/(\lambda_1^2 - \lambda_2^2) \sim 370 \text{ rad m}^{-2}$ . We assume RMs with the minimal absolute values as relevant. RMs calculated that way are displayed in Figure 4 (top panel). All pixels with polarized intensity smaller than the  $3 \times \sigma$ -level, which is about 36 mK at 2695 MHz and 1.5 mK at 4800 MHz, were not included for the RM calculation. The intrinsic polarization angles  $\psi_0$  were then determined based on RM. The orientation of magnetic fields perpendicular to the line of sight, or transverse magnetic fields, is also shown in Figure 4. The transverse magnetic fields nearly follow shell C and are almost perpendicular to shell B, which is consistent with the results by Mantovani et al. (1985).

The RM map exhibits clear patterns as can be seen from Figure 4. For shell structure C, RM changes from positive values towards the southeast to negative values towards the northwest, where the transition is around Galactic latitude  $b = 2.7^\circ$ , which confirms the results by Mantovani et al. (1985). The RM distribution is fairly smooth for the positive RM-area with an average of about  $+60 \text{ rad m}^{-2}$ . For the higher latitude area, the part encompassing the pulsar and its PWN has an average RM of about  $-150 \text{ rad m}^{-2}$ , which is close to the RM of the pulsar PSR B1951+32. The remaining part further northwest has an average RM of about  $-60 \text{ rad m}^{-2}$ .

The RM distribution towards CTB 80 consists of contributions from the Galactic medium in front of the SNR ( $RM_{\text{fg}}$ ) and the medium local to the SNR ( $RM_{\text{snr}}$ ), which can be written as  $RM = RM_{\text{fg}} + \frac{1}{2}RM_{\text{snr}}$ . Here  $RM_{\text{snr}}$  represents the integral of the line-of-sight magnetic field weighted by the thermal electron density over the whole SNR, and the factor  $\frac{1}{2}$  comes from the assumption that the thermal gas and emitting medium are uniformly mixed (e.g. Sokoloff et al. 1998). In contrast, the RM of PSR B1951+32 can be expressed as  $RM_{\text{psr}} = RM_{\text{fg}} + fRM_{\text{snr}}$ , where the factor  $f$  depends on the relative location of the pulsar inside the SNR along the line of sight. If the pulsar sits in the middle of the emitting area, we would expect  $f$  to be  $\frac{1}{2}$ .

The foreground RM can be estimated from pulsars and simulations. We retrieved pulsars within  $10^\circ$  of PSR B1951+32 from the ATNF pulsar catalog<sup>4</sup> (Manchester et al. 2005), and plotted RM and DM against distance in Figure 5. The distances were calculated from DM according to the electron density model by Yao et al. (2017). For pulsar PSR B1951+32, we applied a distance of 2 kpc, the same as for CTB 80. DM is defined as the integral of electron density along the line of sight from the source to the observer. Assuming a uniform distribution of electron density and magnetic field, both DM and RM are expected to have a linear relation with distance. This is roughly the case for DM, which can be seen from Figure 5. However, RM is complicated by a large scatter. For the four pulsars with distances less than 2 kpc, their RM values are:  $-18 \text{ rad m}^{-2}$ ,  $-35 \text{ rad m}^{-2}$ ,  $-75 \text{ rad m}^{-2}$  and  $+26 \text{ rad m}^{-2}$  in the order of increasing distances. The average RM for the four pulsars is about  $-26 \text{ rad m}^{-2}$  with a large standard deviation of about  $36 \text{ rad m}^{-2}$ . We also run simulations of 3D Galactic RM towards  $(l, b) = (69^\circ, 2.7^\circ)$  with the models of Galactic magnetic fields developed by Sun & Reich (2010), and obtained a profile

<sup>4</sup> <https://www.atnf.csiro.au/research/pulsar/psrcat/>

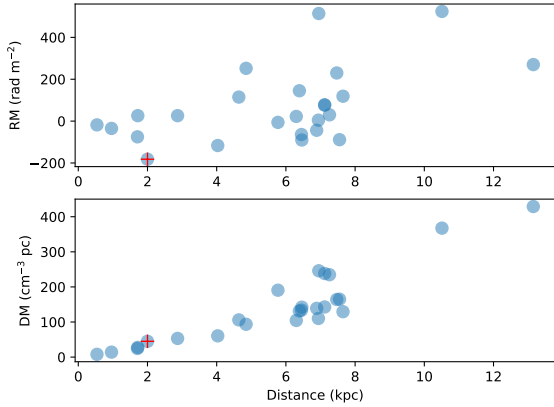


**Fig. 5** RM and DM versus distance for pulsars within  $10^\circ$  of PSR B1951+32 which is marked by a cross.

of RM versus distance from the average within a radius of  $2^\circ$ . The profile shows that the foreground RM is about  $-40 \text{ rad m}^{-2}$  at a distance of 2 kpc. Below, we use a value of  $-30 \text{ rad m}^{-2}$  for  $\text{RM}_{\text{fg}}$ , which is roughly the average of the estimates from the pulsars and the simulations. It should be emphasized here that  $\text{RM}_{\text{fg}}$  is uncertain though.

Based on the RM of CTB 80 (Fig. 4) and  $\text{RM}_{\text{fg}}$ , we obtain a value of about  $-240 \text{ rad m}^{-2}$  for  $\text{RM}_{\text{SNR}}$  of the area near PSR B1951+32, falling in the range estimated from depolarization analysis. For PSR B1951+32, we can derive the  $f$  value of about  $\frac{5}{8}$ , slightly larger than  $\frac{1}{2}$ , meaning that the pulsar is located further than the middle of the emitting medium along the line of sight. For the lower part of shell C, the resulting  $\text{RM}_{\text{SNR}}$  is about  $+180 \text{ rad m}^{-2}$ . This value is expected to cause large depolarization at 2695 MHz, which is not seen from the depolarization map in Fig 3. Thus, synchrotron emission and thermal gas cannot be mixed. A Faraday screen with an RM of about  $+90 \text{ rad m}^{-2}$  in front of the synchrotron emission of the lower part of C can explain the observations.

The change of RM signs for SNRs was reported previously for the SNR CTA 1 (Sun et al. 2011) and SNR G296.5+10.0 (Harvey-Smith et al. 2010). The former was interpreted by the influence of a foreground cloud in accordance with RMs of extragalactic sources, and the latter was attributed to the toroidal field generated by stellar wind from the progenitor star. In the case of CTB 80, the foreground RM is small. However, the large positive RMs in the lower part of shell C could be attributed to the thermal gas inside the SNR but in front of the emitting medium, which acts as a Faraday screen. There are no anomalies from RMs of extragalactic sources towards this area when investigating the Galactic foreground RM map by Oppermann et al. (2015). The reason could be that

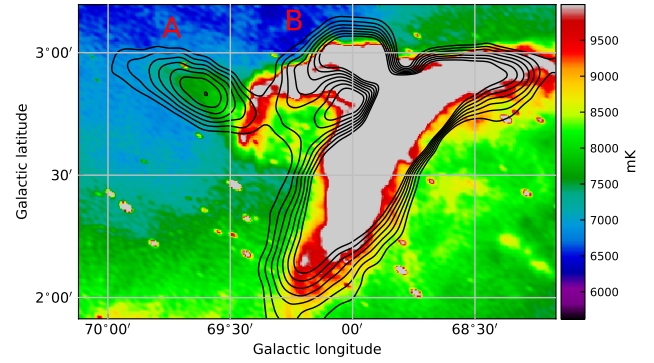


**Fig. 6** Polarized intensity at 4800 MHz in contours overlaid on the total intensity image at 1420 MHz. The levels of the contours go from 8 mK to 20 mK in steps of 2 mK in main beam brightness temperature.

this foreground map was constructed mainly from the RM catalog by Taylor et al. (2009) with a source density of about 1 per square degree, and is therefore not sensitive to RM variations over smaller scales as in shell C. For CTB 80, the sign change occurs within one shell, and the second scenario thus cannot work. Kothes & Brown (2009) demonstrated that the sign of RM changes along the shell of an SNR, in particular when the angle between the magnetic field and the line of sight is small. This seems possible because the location of CTB 80 is close to the strong Cygnus X region, which results from the tangential view along the local arm with the magnetic field aligned.

### 3.4 The Nature of Structure A

The partial shell structure A (Fig. 1) is very intriguing. We overlaid the contours of the polarized intensity at 4800 MHz onto the high resolution total intensity image at 1420 MHz in Figure 6. CTB 80 has an unusual and complex morphology compared to other SNRs and its full extent is not very clear. Whether the faint but highly polarized structure A is part of CTB 80 or not is difficult to decide. With regard to total intensity, it seems that shell B bends towards longitudes larger than about  $69.4^\circ$  to form a quasi-circular shell, whereas shell A is roughly perpendicular to shell B. The non-smooth transition of emission from shell A to shell B suggests that shell A might not be related with shell B and thus CTB 80. The polarized emission from structure A (Fig. 6) appears to be separated from CTB 80. However, the end of the total-intensity shell B is seen in superposition with shell A in the unpolarized area that may indicate depolarization. In fact, Mavromatakis et al. (2001) found faint emission in  $\text{H}\alpha$  +  $[\text{N II}]$  and  $[\text{S II}]$  in this area. This signifies the existence of ionized matter which might cause depolarization through

Faraday effects. In the case that depolarization took place, shell A would be located behind shell B and might be connected to the stronger filaments or shells of CTB 80.

Both shell B and shell C are partly fueled by receiving high-energy particles from PSR B1951+32 and its PWN (e.g. Castelletti & Dubner 2005). Since structure A is further apart, we would expect its spectrum to be similar or steeper than that of shell B or C. This contradicts our result where structure A has a flatter spectrum. The flattening of a spectrum could be caused by strong compression by interaction with the interstellar medium. The flux-density spectral index can be connected to the shock compression ratio  $r$  following  $\alpha = -3/2(r - 1)$  (Reynolds et al. 2012). Given  $\alpha = -0.2$  for structure A, the corresponding ratio is about 8.5. However, there is no indication of high density clumps towards this area from high-resolution H I observations (Park et al. 2013), meaning that this scenario is unlikely. It is therefore possible that shell A is a separate SNR, or part of it, independent of CTB 80.

Mavromatakis et al. (2001) presented CCD images of CTB 80 in several optical lines and discovered a number of long and thin filaments in this area. They concluded that CTB 80 is more extended than earlier radio observations indicated. Lynds Bright Nebula (LBN, Lynds 1965) 156 and 158 are also located in the area of CTB 80, manifesting a complex filamentary structure in their surroundings, which complicates a clear identification of structure A. Mavromatakis & Strom (2002) found shock-heated filaments in the northeast of CTB 80, which they regarded as an indication for the existence of another SNR in this area, although its size and shape were not well constrained by the observed filaments. The two longest thin filaments, apparently emerging from LBN 156, run almost parallel to structure A, but at a distance of about 15'. These filaments have very faint radio counterparts. It seems thus possible that shell A is part of the SNR proposed by Mavromatakis & Strom (2002).

#### 4 CONCLUSIONS

We performed a polarization study of SNR CTB 80 considering recent polarization observations at 1420 MHz, 2695 MHz and 4800 MHz. We smoothed the  $I$  and Stokes  $Q$  and  $U$  maps to a common resolution of 10', and derived maps of polarized intensity and polarization angle. Strong depolarization was found at 1420 MHz. We calculated RMs using polarization angles at 2695 MHz and 4800 MHz. The RM map displays a clear sign change towards shell C. The reason for this change is unclear. Combining the RM and depolarization maps, we found that

the RM of CTB 80 contains a contribution from the thermal gas inside CTB 80 but is not mixed with the emitting medium. We also identified a bright polarized structure with a very weak total-intensity correspondence, which could be either a part of CTB 80 or a part of another SNR independent of CTB 80.

**Acknowledgements** XL and XS are supported by the National Natural Science Foundation of China (Grant No. 11763008). XG is supported by the CAS-NWO cooperation programme (Grant No. GJHZ1865) and the National Natural Science Foundation of China (Grant No. U1831103). We thank Dr. Patricia Reich for reading the manuscript and discussions. We also thank the referee for critical comments that have improved the paper.

#### References

- Anderson, L. D., Armentrout, W. P., Luisi, M., et al. 2018, *ApJS*, 234, 33
- Angerhofer, P. E., Strom, R. G., Velusamy, T., et al. 1981, *A&A*, 94, 313
- Becker, R. H., Helfand, D. J., & Szymkowiak, A. E. 1982, *ApJ*, 255, 557
- Blair, W. P., Fesen, R. A., Rull, T. R., et al. 1984, *ApJ*, 282, 161
- Castelletti, G., & Dubner, G. 2005, *A&A*, 440, 171
- Castelletti, G., Dubner, G., Golap, K., et al. 2003, *AJ*, 126, 2114
- Duncan, A. R., Reich, P., Reich, W., et al. 1999, *A&A*, 350, 447
- Fesen, R. A., Shull, J. M., & Saken, J. M. 1988, *Nature*, 334, 229
- Gao, X. Y., Han, J. L., Reich, W., et al. 2011, *A&A*, 529, A159
- Green, G. M., Schlafly, E. F., Finkbeiner, D., et al. 2018, *MNRAS*, 478, 651
- Harvey-Smith, L., Gaensler, B. M., Kothes, R., et al. 2010, *ApJ*, 712, 1157
- Hobbs, G., Lyne, A. G., Kramer, M., et al. 2004, *MNRAS*, 353, 1311
- Koo, B.-C., Yun, M.-S., Ho, P. T. P., et al. 1993, *ApJ*, 417, 196
- Kothes, R., & Brown, J.-A. 2009, in *IAU Symposium*, 259, *Cosmic Magnetic Fields: From Planets, to Stars and Galaxies*, eds. K. G. Strassmeier, A. G. Kosovichev, & J. E. Beckman, 75
- Kothes, R., Fedotov, K., Foster, T. J., et al. 2006, *A&A*, 457, 1081
- Kulkarni, S. R., Clifton, T. C., Backer, D. C., et al. 1988, *Nature*, 331, 50
- Landecker, T. L., Reich, W., Reid, R. I., et al. 2010, *A&A*, 520, A80
- Leahy, D. A., & Ranasinghe, S. 2012, *MNRAS*, 423, 718
- Lynds, B. T. 1965, *ApJS*, 12, 163
- Manchester, R. N., Hobbs, G. B., Teoh, A., et al. 2005, *AJ*, 129, 1993
- Mantovani, F., Reich, W., Salter, C. J., et al. 1985, *A&A*, 145, 50
- Mavromatakis, F., & Strom, R. G. 2002, *A&A*, 382, 291

- Mavromatakis, F., Ventura, J., Paleologou, E. V., et al. 2001, *A&A*, 371, 300
- Oppermann, N., Junklewitz, H., Greiner, M., et al. 2015, *A&A*, 575, A118
- Park, G., Koo, B. C., Gibson, S. J., et al. 2013, *ApJ*, 777, 14
- Reich, W. 1982, *A&AS*, 48, 219
- Reich, W., Fuerst, E., Reich, P., et al. 1990, *A&AS*, 85, 633
- Reich, W., Fürst, E., Reich, P., et al. 2004, in *The Magnetized Interstellar Medium*, eds. B. Uyaniker, W. Reich, & R. Wielebinski, 45
- Reynolds, S. P., Gaensler, B. M., & Bocchino, F. 2012, *Space Sci. Rev.*, 166, 231
- Safi-Harb, S., Ogelman, H., & Finley, J. P. 1995, *ApJ*, 439, 722
- Shan, S. S., Zhu, H., Tian, W. W., et al. 2018, *ApJS*, 238, 35
- Sokoloff, D. D., Bykov, A. A., Shukurov, A., et al. 1998, *MNRAS*, 299, 189
- Strom, R. G., Angerhofer, P. E., & Dickel, J. R. 1984, *A&A*, 139, 43
- Sun, X.-H., & Reich, W. 2010, *RAA (Research in Astronomy and Astrophysics)*, 10, 1287
- Sun, X. H., Reich, W., Wang, C., et al. 2011, *A&A*, 535, A64
- Taylor, A. R., Stil, J. M., & Sunstrum, C. 2009, *ApJ*, 702, 1230
- Taylor, A. R., Gibson, S. J., Peracaula, M., et al. 2003, *AJ*, 125, 3145
- Tung, A. K., Kothes, R., Landecker, T. L., et al. 2017, *AJ*, 154, 156
- Turtle, A. J., Pugh, J. F., Kenderdine, S., et al. 1962, *MNRAS*, 124, 297
- Velusamy, T., & Kundu, M. R. 1974, *A&A*, 32, 375
- Wardle, J. F. C., & Kronberg, P. P. 1974, *ApJ*, 194, 249
- Weisberg, J. M., Cordes, J. M., Kuan, B., et al. 2004, *ApJS*, 150, 317
- Xiao, L., Han, J. L., Reich, W., et al. 2011, *A&A*, 529, A15
- Yao, J. M., Manchester, R. N., & Wang, N. 2017, *ApJ*, 835, 29